Contents lists available at ScienceDirect

Surfaces and Interfaces

Photoelectrochemical water splitting with dual-photoelectrode tandem and parallel configurations: Enhancing light harvesting and carrier collection efficiencies

Reza Keshavarzi [a,*], Mahlasadat Mousavian [a], MirKazem Omrani [b], Valiollah Mirkhani [a], Niloufar Afzali [a], Camilo A. Mesa [c], Iraj Mohammadpoor-Baltork [a], Sixto Gimenez [c,*]

[a] Department of Chemistry, University of Isfahan, Isfahan 81746-73441, Iran
[b] Department of Physics, University of Isfahan, Isfahan 81746-73441, Iran
[c] Insitute of Advanced Materials (INAM), University Jaume I, Castello de la Plana 12006, Spain

ARTICLE INFO

ABSTRACT

Photoelectrochemical (PEC) water splitting stands out as one of the most promising technologies to store solar energy into chemical bonds and decarbonize industry and transport. In the present study, we develop hetero-structured BiVO$_4$/WO$_3$ and TiO$_2$/PANi photoanodes for water oxidation, aiming at maximizing their spectral activity and their light harvesting efficiency, rationalized by a detailed optical modeling of the PEC cell. Furthermore, we implement tandem and parallel dual-photoelectrode configurations to enhance the collection efficiency. Photocurrents of 1.68 and 2.29 mA/cm^2 at 1.23 V vs RHE were obtained for tandem and parallel configurations, respectively, demonstrating an enhancement factor 4–6 for Tandem and Parallel cells.

1. Introduction

Solar energy has been studied for years as a reliable alternative to fossil fuels and has shown great potential for the future of clean and sustainable energy. The direct conversion of sunlight into chemical fuels in the form of hydrogen (H$_2$) gas is a very promising approach to this end [1,2]. Photoelectrochemical (PEC) water splitting is a powerful strategy, which splits water molecules into hydrogen and oxygen in the presence of sunlight [3]. In PEC water splitting systems, hydrogen evolution reaction (HER) occurs at the cathode (H$^+$/H$_2$ at 0 V vs. reversible hydrogen electrode, RHE) and oxygen evolution reaction (OER) at the anode (O$_2$/H$_2$O at 1.23 V vs. RHE) [4,5]. Although PEC water splitting is a simple process involving (i) the generation of photo-charge carriers (electrons and holes) in semiconductors by sunlight, (ii) their transport to the surface of the corresponding electrodes and (iii) the subsequent transfer to the solution to split water into H$_2$ and O$_2$, there are still many challenges to be solved [2]. The efficiency of these steps determines the activity of the photoelectrode and consequently, optimization of all three of the above steps is needed for the development of an efficient PEC system. Since the primary report on the photoelectrochemical water splitting using TiO$_2$ in 1972, various metal oxide semiconductors have

been extensively studied [6]. TiO$_2$ can only absorb ultraviolet (UV) light (- 4% of total solar energy) to produce electron-hole pairs, due to its wide band-gap (-3.2 eV) [7]. In contrast, alternative multinary metal oxides like BiVO$_4$ with a 2.4 eV bandgap are promising candidates for water oxidation [8,9]. BiVO$_4$ possesses a suitable valence band (VB) position for the OER and absorbs the sunlight with wavelengths shorter than -520 nm [8,10,11]. Due to the poor charge transfer kinetics and slow electron transport, bulk and surface recombination losses need to be minimized, and consequently, BiVO$_4$ is often heterostructured with other semiconductor materials to orthogonalize light absorption and carrier diffusion. Since the first reports on the WO$_3$/BiVO$_4$ hetero-junction nanostructure by Su et al. [12]., and Hong et al. [13], in which BiVO$_4$ mainly acts as a visible light absorber and WO$_3$ as a selective contact for electrons, several studies have been carried out to optimize its performance [14]. WO$_3$ improves the photocurrent, because the fast charge injection to WO$_3$ facilitates the extraction of electrons from BiVO$_4$ [14]. Similarly, a porous structure is desirable to increase the light absorption efficiency of BiVO$_4$, while minimizing carrier diffusion [15].

Kim et al. introduced a hetero-type dual photoelectrode comprised of modified BiVO$_4$ (NiOOH/FeOOH/H$_2$ treated Mo-doped BiVO$_4$) as the

---

* Corresponding authors.
  E-mail addresses: R.Keshavarzi@chem.ui.ac.ir (R. Keshavarzi), sjulia@fca.uji.es (S. Gimenez).

front and a modified Fe_2O_3 (Ni_2FeO_x/H_2 treated TiO_2/Ti-doped Fe_2O_3) as the back photoanodes for extended light-harvesting in PEC water oxidation. This dual photoelectrode presented a 1.4-fold enhance in photocurrent density in comparison with the single modified $BiVO_4$ photoelectrodes, at 1.23 V_{RHE} in 1 M bicarbonate KCi solution (pH=9.2). However, Fe_2O_3 only harvests visible light up to 610 nm (the longer-wavelength <620 nm photons), becoming inactive at longer wavelengths [16,17].

During the last few years, the polymers which encompass expanded conjugated π-electron systems have attracted a great deal of attention, due to their high absorption coefficients in the visible spectrum, high carrier mobility, and high electrical conductivity. In this context, polyaniline (PANi) has shown a great potential to improve electronic conductivity and solar energy harvesting under visible light up to the near IR. This conductive polymer could be easy prepared, and features low cost and outstanding environmental stability [18,19]. Moreover, PANi could be a suitable candidate to achieve appropriate spectral response for photoelectrochemical performance of those semiconductors like TiO_2, which absorb light wavelengths below 400 nm. In this regard, enhanced charge separation efficiency and light absorption in TiO_2/-PANi improves the PEC performance of this photoelectrode. In fact, the photosensitization of TiO_2 material by conducting PANi plays a crucial role on this improvement.

In this study, we first introduce a WO_3/$BiVO_4$ water splitting single photoanode prepared by sol-gel dip-coating method for the first time. Moreover, we introduce a TiO_2/PANi single photoelectrode including ordered TiO_2 templated film coated by PANi for PEC water oxidation for the first time. These photoelectrodes were used without any co-catalysts, extrinsic doping or additional treatments. Subsequently, we implement

a dual-photoelectrode architecture comprised of a WO_3/$BiVO_4$ as the front and a TiO_2/PANi as the back photoanode. The TiO_2/PANi photoanode is placed behind the WO_3/$BiVO_4$ to use the entire visible range of the solar spectrum and utilize the low-energy photons passing through the initial absorber. TiO_2/PANi can absorb a wide range of photon energies, in particular those regions, where bismuth vanadate is inactive. Moreover, a dual-photoelectrode device, combining the parallel illumination of these two photoanodes was designed and the PEC performance was investigated (Fig. 1 shows the photoelectrode configurations tested in this study). Accordingly, a PEC device including WO_3/$BiVO_4$ and TiO_2/PANi heterodual photoanodes under parallel illumination shows a stable photocurrent of 2.29 mA.cm^2 at 1.23 V_{RHE} (around 6-times higher compared to the photocurrent of the single $BiVO_4$ photoanode) under simulated AM 1.5 G illumination using visible light up to 800 nm. We believe that this study will open the door to new horizons for the exploitation of metal oxide heterostructures.

2. Results and discussion

Single heterostructured WO_3/$BiVO_4$ and TiO_2/PANi water oxidation photoelectrodes were prepared as detailed in the Experimental Method. XRD diffractograms of WO_3, $BiVO_4$ and the corresponding $BiVO_4$ heterojunction (WO_3/$BiVO_4$) coated films on FTO substrates are displayed in Fig. 2a. The monoclinic structure for WO_3 films was confirmed by the main peaks corresponding to the (002), (200) planes at 2θ values of 23.25°, 24.45°, respectively [20]. It is worth mentioning that the monoclinic phase of WO_3 is strongly stable at room temperature and provides larger PEC activity compared to other WO_3 polymorphs [21]. Additionally, XRD peaks at 2θ = 18.9°, 28.9°, 30.5° and 35.2° were attributed to
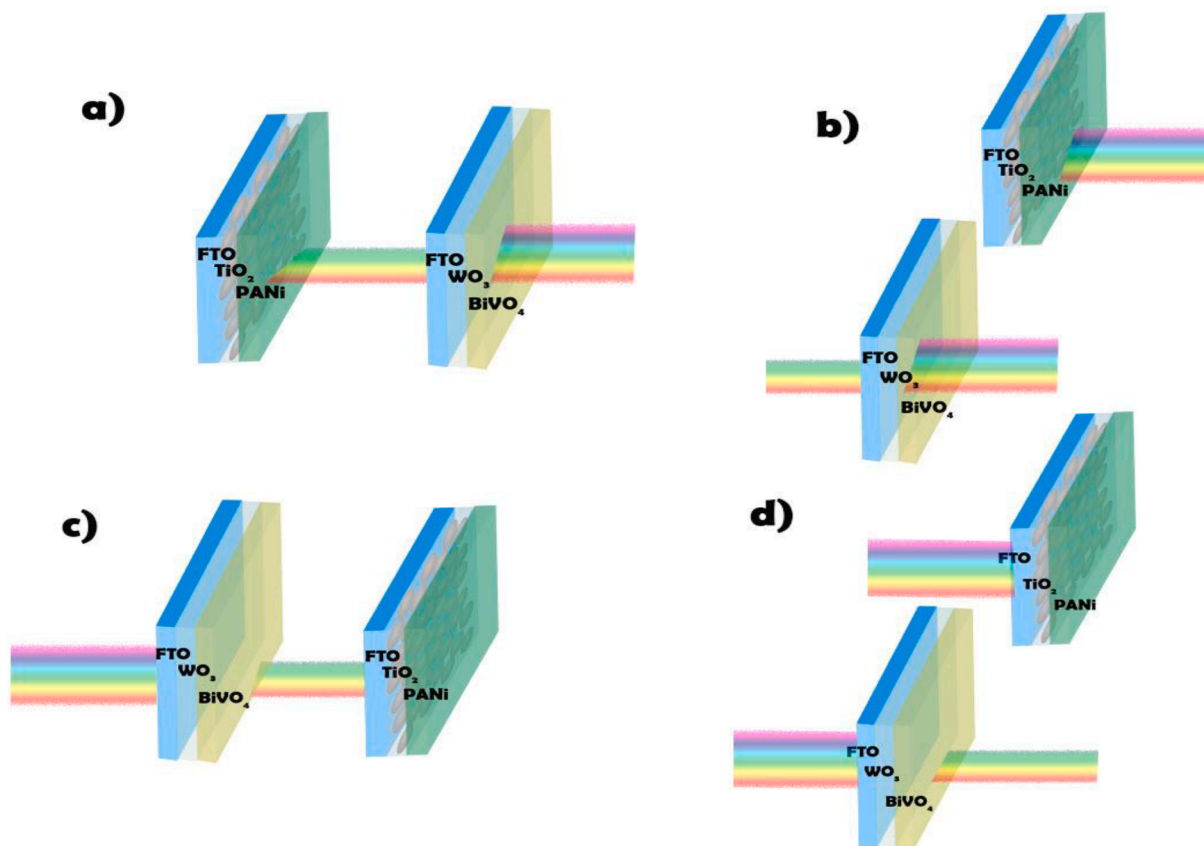
Fig. 1. Scheme of the rationale supporting the dual-photoelectrode configuration for direct PEC water splitting under (a) tandem (front-side illumination), (b) parallel (front-side illumination), (c) tandem (backside illumination), and (d) parallel (backside illumination) modes. In tandem mode, TiO_2/PANi photoanode is placed behind the WO_3/$BiVO_4$ photoelectrode to use the entire visible range of the solar spectrum and utilize the low-energy photons transmitted from the first absorber. In parallel illumination mode, both WO_3/$BiVO_4$ and PANi/TiO_2 photoelectrodes were simultaneously exposed to a solar simulator light source.
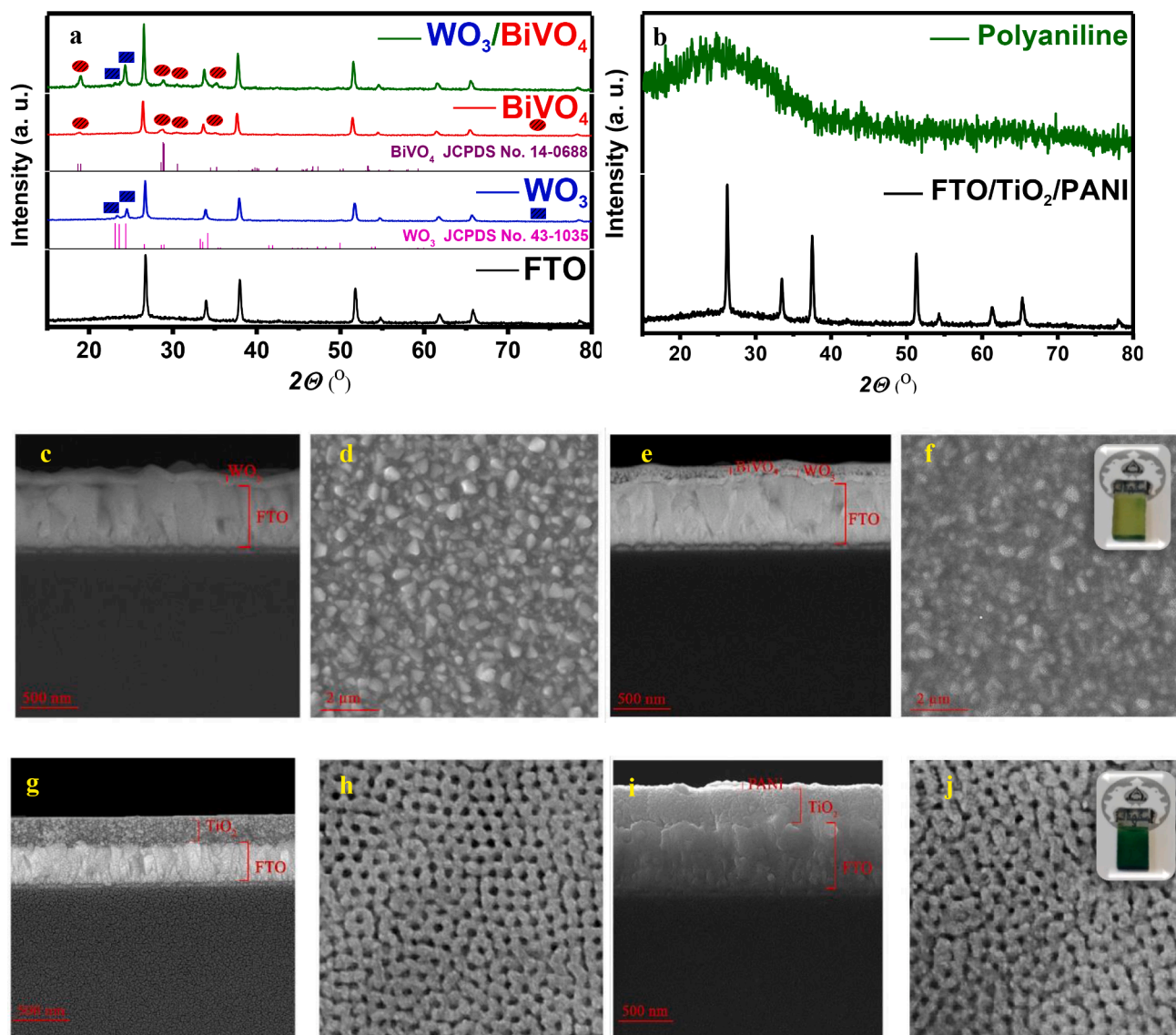
Fig. 2. XRD patterns of a) WO_3, $BiVO_4$, and $WO_3/BiVO_4$ on FTO, and b) $TiO_2/PANi$ coated on FTO, and polyaniline coated glass. The unlabelled diffraction peaks in Fig. 1a are related to the FTO substrate. FE-SEM images of c) WO_3 (cross section), d) WO_3 (top view), e) $WO_3/BiVO_4$ (cross section), f) $WO_3/BiVO_4$ (top view), g) TiO_2 (cross section), h) TiO_2 (top view), i) $TiO_2/PANi$ (cross section), and j) $TiO_2/PANi$ (top view). The insets of Fig. 2f and j show the digital photographs of the $WO_3/BiVO_4$ and $TiO_2/PANi$ electrodes, respectively.

the (011), (121), (040) and (002) planes of monoclinic $BiVO_4$ [22,23]. The unlabeled diffraction peaks are attributed to the FTO substrate. On the other hand, Fig. 2b shows the XRD pattern of polyaniline layer coated on the TiO_2 thin film with FTO substrate. The diffraction peaks of the TiO_2 film are not detected probably due to its high porosity in a thin layer of templated TiO_2 coated on FTO [24,25]. However, a diffraction peak was observed for TiO_2 in a multilayer thick film coated on FTO (Supplementary Information, Figure S1). The peak at $2\theta = 25.3°$ corresponds to the anatas TiO_2 (101) crystal plane. No diffraction peaks were detected for PANi. The XRD pattern of PANI thin films on glass reveals a broad peak at $2\theta = 22.68°$, confirming its amorphous nature [26]. Furthermore, no crystalline impurities were detected by XRD analysis.

The cross-section FE-SEM images of the WO_3, and $WO_3/BiVO_4$ photoanodes are shown in Fig. 2c and e, respectively. The top view FE-SEM image of WO_3 film (Fig. 2d) shows a dense nanoparticulated layer on the FTO substrate without the presence of any pinholes or cracks. Two distinct layers of WO_3 and $BiVO_4$ can be clearly identified on top of the FTO in $WO_3/BiVO_4$ structure, with approximate thicknesses of around 65 and 115 nm, respectively. The optimum thickness for each

layer was achieved by varying the withdrawal rates of dip coating as shown in Fig. S2. Contrary to the WO_3 layer, the $BiVO_4$ film coated on WO_3 presents interconnecting "wormlike" branches with high porosity, as observed in Fig. 2e, 2f, and Supplementary Information, Fig. S3 at higher magnification.

Fig. 2g shows a cross-section FE-SEM image of TiO_2 film coated on FTO with a thickness of around 200–280 nm. A well-ordered morphology with open pores is obtained by the use of P123 block copolymer as a template (see top view, Fig. 2h). The deposition of PANi on the TiO_2-ordered mesoporous templated films did not change the morphology, as observed in the top view image, (Fig. 2j) demonstrating that the coated polyaniline material on the titania film is ultra-thin.

EDS analysis confirms the presence of Ti, and O in the $TiO_2/PANi$ layer coated on FTO glass (Supplementary Information, Fig. S4). According to the elemental maps of the cross-sectional image of $TiO_2/PANi$ film (Supplementary Information, Fig. S5) N and C of PANi film is distributed across the entire coating thickness. Supplementary Information, Fig. S6 show the distribution of Si, Sn and Ti on glass/FTO/$TiO_2/PANi$ structure.

Fig. 3a illustrates the absorption spectra of the photoelectrodes. The BiVO$_4$/WO$_3$ photoelectrode is active up to 520 nm. On the other hand, the ordered TiO$_2$ film absorbs light only at wavelengths shorter than 400 nm and possesses an absorption sharp edge near 385 nm. In the case of PANi/TiO$_2$ films, a broad absorption peak appeared from near 400 nm to beyond 800 nm. Interestingly, this heterostructure covers the visible spectral region where BiVO$_4$ alone cannot absorb (520–800 nm). The origin of this broad peak stems from the charge carrier delocalization at PANi [27].

To evaluate the optimal illumination conditions for the developed heterostructured photoelectrodes, J-V curves of the single films including TiO$_2$/PANi and WO$_3$/BiVO$_4$ were measured under the front and back side AM.1.5 G illumination (Supplementary Information, Figure S7). As observed, all photoelectrodes exhibited higher photocurrent density at 1.23 V$_{RHE}$ under back illumination compared to front illumination. Various reasons have been suggested for this behavior. BiVO$_4$ possesses slow water-oxidation kinetics [10]. The electron-hole pairs are created closer to the electrode/electrolyte interface in front-side illumination, and holes reach the surface quickly, while electrons must be transported the entire pathway to the FTO conductive substrate. Lower photocurrent for illumination at the front-side, indicates that electron transport is a key limiting factor [11,28]. For WO$_3$/BiVO$_4$, a large fraction of light could be absorbed by BiVO$_4$ material under front illumination. However, high current density could not
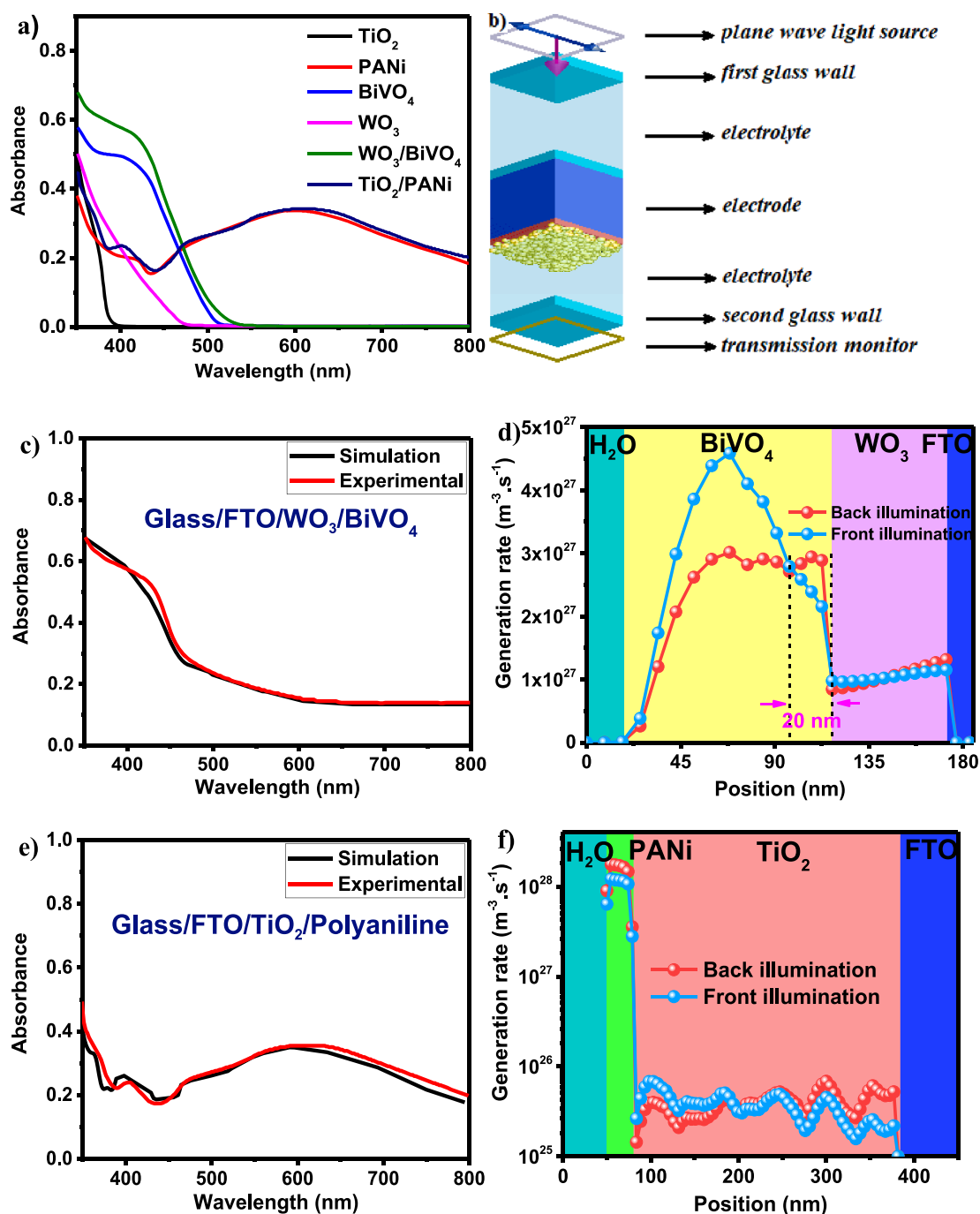
Fig. 3. (a) UV–Vis absorption diagrams of TiO$_2$/PANi, PANi, WO$_3$/BiVO$_4$, BiVO$_4$, WO$_3$ and TiO$_2$ films, (b) The schematic image of the designed configuration for the optical simulation. Absorbance spectra of the simulated and fabricated (c) Glass/FTO/WO$_3$/BiVO$_4$ and e) Glass/FTO/TiO$_2$/PANi electrodes. Spatially varying exciton generation rates of (d) Glass/FTO/WO$_3$/BiVO$_4$ and f) Glass/FTO/TiO$_2$/Polyaniline electrodes.

be achieved due to the restriction of charge transport rate through the BiVO$_4$ layer and WO$_3$/BiVO$_4$ interface. (Supplementary Information, Fig. S7b).

Although some studies have been focused on the electrode performance as a function of the illumination conditions (back and front side illumination), numerical simulations or experimental studies have not provided any direct evidence proving the reasons for the observed behavior. To provide a clear assessment on the effect of the illumination conditions on the electrode behavior, we have simulated the Glass/FTO/WO$_3$/BiVO$_4$ structure using the Finite-Difference Time-Domain (FDTD) method. In the simulation process, the electrode is placed inside an electrolyte medium (n = 1.33) and the effect of a glass container used in practice for the spectroscopy of the sample is considered. Since the absorption spectrum is measured using the UV–Visible transmission technique, light reflections from the walls of the glass container (in which the electrodes have been immersed inside the electrolyte) during spectroscopy appear as errors in the sample absorption spectrum. The resulting error in the absorption spectrum, which does not lead to the generation of photocarriers, can be clearly seen by comparing Supplementary Information, Figure S9 with Fig. 3a. A propagated plane wave light along the z-axis and in the air environment first passes through the first glass wall and enters the electrolyte environment. After interaction with the electrode and passing through the electrolyte and second glass wall, the transmission spectrum is calculated by the placed frequency-domain transmission monitor, as shown in Fig. 3b. Periodic and perfectly matched-layer (PML) boundary conditions are applied in the in-plane directions and the z-direction, respectively. First, FTO and WO$_3$ layers have been added to the Glass with thicknesses of 660 and 60 nm, respectively. Then, the porous BiVO$_4$ layer was modeled using deformed nanoparticles with size distributions taken from FE-SEM images. With a porosity of 29% (derived from the ellipsometry analysis), the nanoparticles are randomly distributed along the desired layer volume. In this case, a simulation with minimal error compared to experimental results is provided with regard to considering the scattered light during the incident light interaction with the porous BiVO4 layer.

Fig. 3c shows the absorption spectrum measured from the fabricated electrode compared to the simulation results. The absorption spectrum is calculated from the transmission spectrum using the equation, *Absorbance* = 2 − *log*(*Transmittance*%) [29]. The calculated absorption spectrum is in good agreement with the experimental spectrum, which shows that the modeling performed in this work can accurately describe the optical characteristics of the device. The distribution of exciton generation rate along the WO$_3$/BiVO$_4$ structure has been calculated under the back and front sides with AM 1.5 G illumination (Fig. 3d). The following equations were used to calculate the exciton generation rate [30]:

$$P_{abs} = -0.5\Re(\nabla.\mathbf{P}) = -0.5\omega|\mathbf{E}|^2\mathfrak{I}(\varepsilon) \tag{1}$$

$$g = \frac{P_{abs}}{\hbar\omega} = -\frac{0.5}{\hbar}|\mathbf{E}|^2\mathfrak{I}(\varepsilon) \tag{2}$$

$$G = \int\int g(\omega)d\omega dV \tag{3}$$

where P_{abs}, G, g, $\mathbf{P}$, ε and ω are the power absorption, total number of produced charge carriers, exciton generation rate (assuming that each photon produces one exciton), Poynting vector, the permittivity, and the angular frequency, respectively.

Under front illumination, although a high rate of the excitons is generated inside the BiVO$_4$ layer, lower photocurrent density is obtained compared to back illumination (Supplementary Information, Fig. S7b). In these conditions, a large fraction of incident light is absorbed near the BiVO$_4$/electrolyte interface and produces excitons. Conversely, with back illumination, more excitons are generated in the vicinity of the WO$_3$/BiVO$_4$ interface compared to the front illumination. However, under front illumination, the photogenerated electrons have to travel long distances to reach the WO$_3$ layer, whereas their diffusion length is

limited by the porous structure of the BiVO$_4$ layer. On the other hand, the pores inside the structure of porous BiVO$_4$, which has been filled by the electrolyte solution, allow the holes to move much shorter distances to meet the electrolyte. This in turn reduces the photocurrent density owing to the bulk recombination of electrons traveling to WO$_3$. In contrast, under back illumination, most of the excitons generated at the vicinity of the WO$_3$/BiVO$_4$ interface experience a charge separation process, and the electrode exhibits a higher photocurrent density. Similar calculations were performed for the electrode with Glass/FTO/TiO$_2$/PANi structure (Fig. 3e). This heterostructure also shows a higher photocurrent density under back illumination (Supplementary Information, Figure S7c), due to the higher rate of exciton generation at the vicinity of the FTO/TiO$_2$ interface (Fig. 3f) and therefore, higher charge separation efficiency. However, the PEC performance of PANi directly coated on FTO is shown in Figure S8 for comparison with TiO$_2$/PANi.

The photoelectrochemical activities of single and dual films under back-side illumination are presented in Fig. 4a. The water oxidation photocurrents of BiVO$_4$, TiO$_2$/PANi, WO$_3$/BiVO$_4$, and dual photoelectrodes (Tandem and Parallel illumination) were 0.40, 0.86, 1.20, 1.68, and 2.29 mA/cm^2 at 1.23 V$_{RHE}$, respectively. As a result, although WO$_3$/BiVO$_4$ heterojunction sample shows three times as much photocurrent as the BiVO$_4$ control, dual photoelectrodes exhibit far higher currents, around 4 and 6 times higher for tandem and parallel cells, respectively. The bumps observed for the dual parallel configuration are believed to be related to the formation and elimination of O$_2$ bubbles at this higher photocurrent.

Compared to BiVO$_4$, the higher photocurrent density of the heterostructured WO$_3$/BiVO$_4$ photoelectrode is related to the fast charge transfer into WO$_3$, which facilitates the extraction of electrons from BiVO$_4$ [14]. This is confirmed by the lower photoluminescence (PL) obtained from WO$_3$/BiVO$_4$ compared to the reference BiVO$_4$. (Supplementary Information, Fig. S10a). Similar results can be observed for the TiO$_2$/PANi photoelectrodes (Supplementary Information, Fig. S10b). The higher photocurrent of WO$_3$/BiVO$_4$ and TiO$_2$/PANi illustrates the increased lifetime and charge separation efficiency of the photogenerated charge carriers through the interaction between BiVO$_4$ and WO$_3$ as well as TiO$_2$ and PANi materials. The dual electrode with tandem illumination mode with a current of 1.68 mA/cm^2 showed better performance compared to the single electrodes. This is ascribed to the absorption of those light wavelengths passing through the WO$_3$/BiVO$_4$ front electrode and absorbed by TiO$_2$/PANi back electrode. However, for hetero dual photoanodes with a wide light absorption range, the parallel illumination mode exhibits higher efficiency compared to those under tandem illumination and the reported single electrodes [11,31]. The higher efficiency of parallel mode is probably related to its larger driving force for water splitting reaction and the smaller photovoltage loss [32].

To further evaluate the photoresponse of the samples, IPCE measurements were carried out at 1.23 vs RHE (Fig. 4b). Both the BiVO$_4$ and WO$_3$/BiVO$_4$ photoanodes show an onset wavelength at -520 nm. The WO$_3$/BiVO$_4$ photoanode exhibits significantly higher IPCE performance (i.e., 42.8%) at -380 nm, while BiVO$_4$ shows IPCE of 25.7% at -380 nm suggesting enhanced charge separation efficiency with the presence of WO$_3$ layer. An IPCE onset wavelength at -800 nm is observed for TiO$_2$/PANi and dual photoelectrodes, in good agreement with their corresponding UV–Vis absorbance spectra (Fig. 3a). TiO$_2$/PANi, tandem and parallel dual photoelectrodes present maximum IPCEs of 29.9%, 48.2%, and 54.3% at -380 nm, respectively, due to enhanced charge separation efficiency and light absorption in these samples. Importantly, the photosensitization of TiO$_2$ ordered films with conducting PANi plays a crucial role on the improvement of the related IPCE activities [19,33]. The change of slope systematically observed between 430 and 480 nm for all samples is believed to be due to a small artifact stemming from the photodetector employed for the calibration of our system. In any case, integrated photocurrents from IPCE spectra were calculated showing excellent agreement with photocurrent values reported in Fig. 4a. The
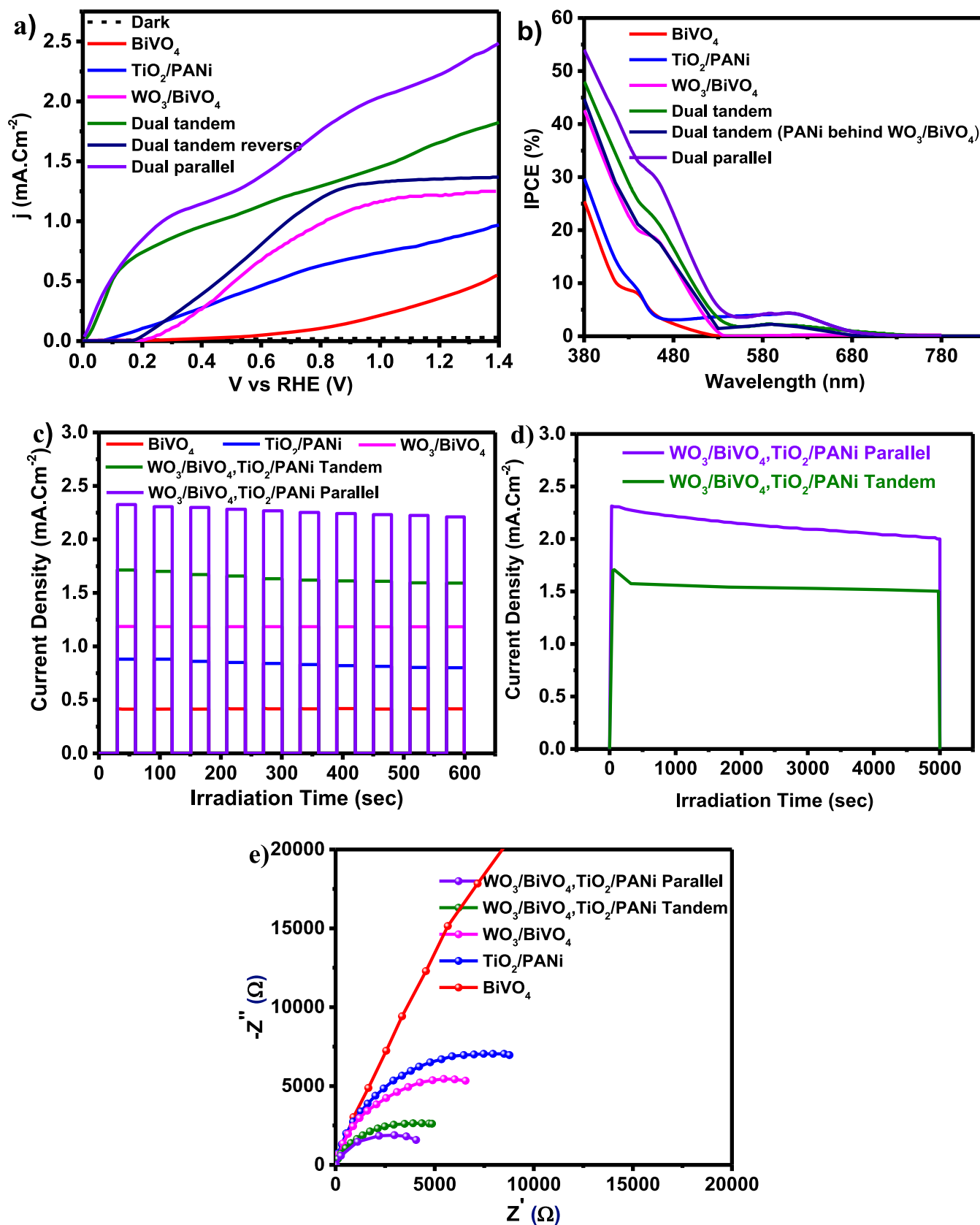
Fig. 4. (a) J–V diagram of $BiVO_4$, TiO_2/PANi, WO_3/$BiVO_4$, and dual electrodes (Tandem and parallel illumination modes), (b) IPCE diagram of $BiVO_4$, TiO_2/PANi, WO_3/$BiVO_4$, and dual electrodes (Tandem and parallel illumination modes), (c) Transient photocurrent measurements for PEC water oxidation reaction with $BiVO_4$, TiO_2/PANi, WO_3/$BiVO_4$, and dual electrodes (Tandem and parallel illumination modes), (d) chronoamperometry of parallel and tandem dual electrodes at 1.23 V vs. RHE, and (e) Nyquist plots of the photoanodes at 0.6 V_{RHE}.

integrated photocurrents of BiVO$_4$, TiO$_2$/PANi, WO$_3$/BiVO$_4$, and dual photoelectrodes (Tandem and Parallel illumination) were 0.40, 0.87, 1.21, 1.69, and 2.31 mA/cm^2 at 1.23 V$_{RHE}$, respectively.

Fig. 4c shows the chronoamperometric measurements under chopped AM1.5 G illumination at 1.23 V$_{RHE}$. Consistently with J-V curves, these measurements also proved that tandem and parallel photoelectrodes have remarkably improved photocurrent densities and possess fast and reusable photocurrent with no noticeable degradation after 10 min. However, the performance of PANi-containing electrodes decreases with a slow slope over time. This is related to the degradation of the PANi polymer due to oxidation.

Fig. 4d shows a chronoamperometric measurement under constant illumination, for 100 min, at 1.23 V$_{RHE}$ for the parallel dual photoelectrode and presents a notable stability. A relative 12% photocurrent loss was measured after 100 min.

To investigate the charge-transfer kinetics at the semiconductor/ electrolyte interface electrochemical impedance measurements were performed at 0.6 V vs RHE. The corresponding Nyquist plots are shown as Fig. 4e. All measurements show an arc, whose radius is attributed to the charge transfer resistance through the semiconductor/electrolyte interface [34,35]. The largest charge transfer resistance is attributed to BiVO$_4$ while this resistance is significantly reduced for the electrode with parallel illumination mode, demonstrating that the charge transfer kinetics at the dual electrode/electrolyte interface is improved efficiently by designing both heterojuction with WO$_3$ and adding TiO$_2$/- PANi wide light absorber electrode, in accordance with the related PEC performances. Furtheremore, the LSV and IPCE data of WO$_3$, TiO$_2$, WO$_3$ behind BiVO$_4$ tandem, and TiO$_2$ behind PANi tandem system are shown in Figure S11. Figure S10.

Fig. 5 shows the proposed band diagram of the WO$_3$/BiVO$_4$ and TiO$_2$/PANi heterostructures explaining the charge transfer steps during illumination leading to the PEC oxidation of water [22,36,37].

Both energy diagrams exhibit a type II heterostructure and consequently, the photoexcited electrons at BiVO$_4$ are injected into the conduction band of WO$_3$ and then driven into FTO under applied potential. Simultaneously, the transport of holes takes place from WO$_3$ to BiVO$_4$ leading to efficient charge separation, reducing the recombination process and inducing enhanced PEC performance. The holes injected into BiVO$_4$ and driven to the surface can participate in water oxidation. Regarding the TiO$_2$/PANi photoelectrode, a similar type II heterostructure is formed. Consequently, upon UV–vis light illumination, the excitation of electrons simultaneously occurs at both PANi and TiO$_2$. The photogenerated electrons are injected from the LUMO of PANI to the CB of TiO$_2$ and are then collected at the FTO substrate. On the other hand,

the photogenerated holes will be driven in the opposite direction from the VB of TiO$_2$ to the HOMO of PANI, leading to spatial charge separation. The TiO$_2$ CB (PANI HOMO) is populated with a high density of electrons (holes), owing to the proper band alignment and the efficient charge separation. These holes driven to the interface with the liquid electrolyte can participate in the water oxidation reaction. The optical absorbance at 800 nm for PANi (2.65 eV bandgap) can be explained by several factors like (i) Charge delocalization [20], polaron/bipolaron transitions caused by the interband charge transfer from benzoid to quinoid rings, and donor–acceptor interaction between the quinoid fragments and the counteranion together with the creation of dopant levels created inside the band gap by acid doping [38,39]. This behavior is consistent with our photoluminescence spectra shown in Fig. S10.

3. Experimental section

3.1. Synthesis of WO$_4$/BiVO$_4$ photoelectrode

3.1.1. Synthesis of WO$_3$ thin films

First, tungsten hexachloride (WCl$_6$, anhydrous) and dried ethanol were mixed in a closed flask under an inert atmosphere such as nitrogen and a solution was prepared. The solution was stirred for 1 day and then refluxed at 45–50 °C for 24 h. Next, the solution was released into the air until the blue color vanished and then filtered to separate the solid precipitate. To prepare WO$_3$ layers the solution was coated on FTO substrates by using the dip-coating method at the withdrawal speed of 120 mm/min. Finally, the coated film was heated for 10 min at 80 °C and then for 1.5 h at 500 °C (heating rate: 5 °C/min) [40].

3.1.2. Synthesis of biVO$_4$ thin films on WO$_3$

To synthesize the sol BiVO$_4$, a Bismuth nitrate (0.002 mol, 98.0%, Aldrich) was added to a solution of citric acid (0.004 mol, 99.5%, Merck) and nitric acid (6 ml, 23.3%, Merck). After that, Bismuth nitrate (2 mmol, 98%, Merck) and ammonium metavanadate (2 mmol, 99%, Merck) were added to the prepared solution, respectively, and continually stirred. Then, polyvinyl alcohol (PVA) (0.04 g, 99%, Merck) and acetic acid (250 μl, 99%, Merck) were added into the mixture and stirred for 24 h until a clear blue solution was formed. After completion of the reaction, the solution was filtered and the clear sol was deposited by dip-coating. The prepared sol was coated on FTO/WO3 substrates at 20 mm/ min and then heated at 100 °C for 10 min and 500 °C for 1 h, using a heating rate of 5 °C/min [22].
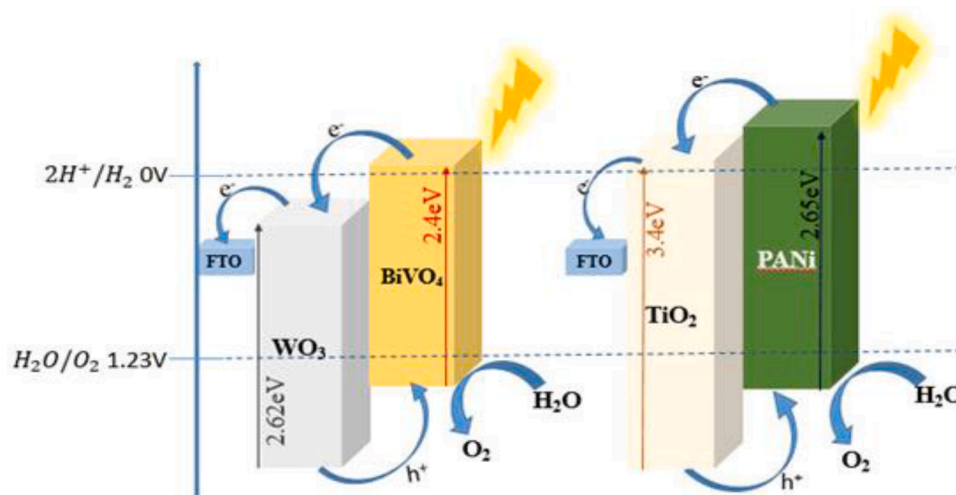

Fig. 5. Schematic diagram for the water oxidation mechanisms in WO$_3$/BiVO$_4$ and TiO$_2$/PANi electrodes. The band positions have been adapted from reported literature [22,36,37].

3.2. Synthesis of tiO₂/PANi photoelectrode

3.2.1. Synthesis of TiO₂ thin films

TiO_2 sol was prepared by slowly and dropwise adding of concentrated hydrochloric acid (9.7 g of) to titanium isopropoxide (12.7 g, 99%, Merck), under rapid stirring. Separately, the P123 copolymer (4 g, 99%, Merck) was dissolved in 1-butanol (36.3 g, 99%, Merck) and then added to the titanium isopropoxide in hydrochloric acid solution. This clear yellow solution is ready to be deposited after stirring for 3 h at room temperature [41,42].

To obtain regular mesoporous TiO_2 films on top of FTO substrates using dip coating, the relative humidity and withdrawal speed of the substrate from the solution were adjusted 25–30% and 0.8 mm/s, respectively. After deposition, the films were transferred to another chamber and kept for 24 h at 75% relative humidity at 20 °C. The prepared layer was heated at 450 °C for 1 h [43].

3.2.2. Synthesis of PANi thin films on TiO₂

To synthesize polyaniline on the prepared TiO_2 films, the prepared films need to be activated. This takes place by putting the prepared layer in a solution of sulfuric acid (0.5 M, 97%, Merck) for 24 h under rapid stirring conditions. After that, the activated TiO_2 film was rinsed twice with distilled water and was heated at 500 °C for 3 h.

The activated films were immersed in a hydrochloric acid solution (2 M, 37%, Merck) and then aniline (1 cc, 99%, Merck) was poured into the solution under rapid stirring and was kept for 24 h. In the final step, $FeSO_4$ solution (5 drops of 5%w, Merck) was added to the solution of HCl / Aniline. Following that, ammonium sulfate solution (10 cc of 5% w, Merck) and solution of Dodecyl Benzene Sulfonic Acid (10 cc of 0.5 M, Merck) were mixed to the above solution with rapid stirring conditions. After 24 h of stirring, the electrodes were washed with double distilled water [44,45].

3.3. Instrumentation

A Shimadzu spectrophotometer was used to obtain UV–vis absorption spectra. A Bruker D8 Advanced instrument using Cu Kα radiation (λ = 1.5406 Å) was employed to record X-ray diffraction (XRD) patterns. To investigate the samples' morphology and thickness, Field emission scanning electron microscopy (FE-SEM, Hitachi S4160, Japan) was used and to determine the elemental composition of the materials Energy-dispersive X-ray spectroscopy (EDS) was applied.

3.4. Photoelectrochemical (PEC) measurements

A three-electrode system was utilized to evaluate the activity of the dual working electrodes. N_2 gas was bubbled into the reaction vessel to remove dissolved O_2 and vigorous stirring was applied to the mixture at room temperature. TiO_2/PANi and WO_3/BiVO₄ films with 1 cm² active size on FTO were used as the working electrode (WE). Platinum (Pt) mesh and Ag/AgCl were employed as the counter electrode (CE) and reference electrode (RE), respectively, in electrolyte solution: 0.5 mol L⁻¹ Na_2SO_4 in water (pH 6.8). PEC measurements were performed by the use of an IM6x electrochemical workstation (Zahner, Germany) to monitor the I/V characteristic in the presence of a solar simulator (AM1.5 G, 100 mW/cm², Optic Niroo). For the parallel configuration, the area of both electrodes (1 + 1 = 2 cm²) was considered to normalize the obtained photocurrent. Electrochemical impedance spectroscopy (EIS) was measured in a frequency range from 0.01 Hz to 100 kHz, by applying a 10 mV AC amplitude under an outer bias voltage of 0.6 V (vs. Ag/AgCl/saturated KCl, equal to 1.23 V_{RHE}). Photocurrent transient measurements were recorded by repeated ON/OFF light with 1 sun illumination at 1.23 V_{RHE}.

5. Conclusion

To enhance the photoelectrochemical performance of BiVO₄ photoanodes for water oxidation, two different heterostructures (WO_3/BiVO₄ and TiO_2/PANi) were prepared. WO3/BiVO4 was prepared to increase the charge carrier separation efficiency. To increase the light-harvesting efficiency, TiO_2/PANi electrode was prepared and used in a dual photoelectrochemical system combined with WO_3/BiVO₄ in tandem and parallel illumination modes. The single films including TiO_2/PANi and WO_3/BiVO₄ exhibited higher photocurrent density at 1.23 V_{RHE} under back illumination (compared to that under front illumination). WO_3/BiVO₄ showed a photocurrent density of 1.20 mA/cm² at 1.23 V_{RHE}, three times higher compared to that for BiVO₄ alone without using any co-catalyst, doping or further post-synthetic treatments. The Tandem configuration of both heterostructured electrodes resulted in a photocurrent density of 1.68 mA/cm² at 1.23 V_{RHE}, significantly higher compared to single electrodes, due to the higher light harvesting efficiency. Finally, the best performance was provided by dual arrangement in parallel illumination mode leading to 2.29 mA/cm² at 1.23 V_{RHE}. The higher driving force for water oxidation as well as lower recombination losses as derived from external quantum efficiency (IPCE) and enhanced charge transfer kinetics (from impedance characterization) are believed to be the reason for this enhanced performance. In summary, this study highlights that tailored architectures combining different absorbers offer a synergistic pathway toward the efficient exploitation of metal oxide heterostructures. Although some hypotheses were presented for the superior efficiency of parallel mode, future studies can investigate more on the mechanism of tandem and parallel configurations.

CRediT authorship contribution statement

Reza Keshavarzi: Conceptualization, Supervision, Methodology, Writing – original draft, Writing – review & editing. **Mahlasadat Mousavian:** Investigation, Methodology, Data curation, Writing – original draft. **MirKazem Omrani:** Visualization, Writing – original draft. **Valiollah Mirkhani:** Investigation, Visualization, Supervision. **Niloufar Afzali:** Investigation, Methodology. **Camilo A. Mesa:** Writing – review & editing, Validation. **Iraj Mohammadpoor-Baltork:** Investigation, Data curation. **Sixto Gimenez:** Conceptualization, Supervision, Writing – review & editing.

Declaration of Competing Interest

The authors declare that they have no known competing financial interests or personal relationships that could have appeared to influence the work reported in this paper.

Data availability

Data will be made available on request.

References

[1] N. Afzali, R. Keshavarzi, S. Tangestaninejad, S. Gimenez, V. Mirkhani, M. Moghadam, I. Mohammadpoor-Baltork, Multifunctional approach to improve water oxidation performance with MOF-based photoelectrodes, Appl. Mater. Today 24 (2021), 101159.

[2] N. Afzali, S. Tangestaninejad, R. Keshavarzi, V. Mirkhani, J. Nematollahi, M. Moghadam, I. Mohammadpoor-Baltork, M. Reimer, S. Olthof, A. Klein,

S. Gimenez, Hierarchical Ti-based MOF with embedded RuO₂ nanoparticles: a highly efficient photoelectrode for visible light water oxidation, ACS Sustain. Chem. Eng. 8 (50) (2020) 18366–18376.

[3] M.G. Walter, E.L. Warren, J.R. McKone, S.W. Boettcher, Q. Mi, E.A. Santori, N. S. Lewis, Sol. Water Split. Cells, Chem. Rev. 110 (11) (2010) 6446–6473.

[4] H. Furukawa, K.E. Cordova, M. O'Keeffe, O.M. Yaghi, The chemistry and applications of metal-organic frameworks, Science 341 (6149) (2013) 1230444.

[5] O.M. Yaghi, M. O'Keeffe, N.W. Ockwig, H.K. Chae, M. Eddaoudi, J. Kim, Reticular synthesis and the design of new materials, Nature 423 (6941) (2003) 705–714.

[6] P. Sharma, J.W. Jang, J.S. Lee, Key strategies to advance the photoelectrochemical water splitting performance of α-Fe₂O₃ photoanode, ChemCatChem 11 (1) (2019) 157–179.

[7] Z. Li, W. Luo, M. Zhang, J. Feng, Z. Zou, Photoelectrochemical cells for solar hydrogen production: current state of promising photoelectrodes, methods to improve their properties, and outlook, Energy Environ. Sci. 6 (2) (2013) 347–370.

[8] U. Prasad, BiVO₄-based photoanodes for photoelectrochemical water splitting, Clean Energy Mater (2020) 137–167.

[9] S.M. Thalluri, C. Martinez Suarez, M. Hussain, S. Hernandez, A. Virga, G. Saracco, N. Russo, Evaluation of the parameters affecting the visible-light-induced photocatalytic activity of monoclinic BiVO₄ for water oxidation, Ind. Eng. Chem. Res. 52 (49) (2013) 17414–17418.

[10] J.R. Ding, K.S. Kim, 1-D WO₃@ BiVO₄ heterojunctions with highly enhanced photoelectrochemical performance, Chem. Eng. J. 334 (2018) 1650–1656.

[11] Y. Park, K.J. McDonald, K.-.S. Choi, Progress in bismuth vanadate photoanodes for use in solar water oxidation, Chem Soc. Rev. 42 (6) (2013) 2321–2337.

[12] J. Su, L. Guo, N. Bao, C.A. Grimes, Nanostructured WO₃/BiVO₄ heterojunction films for efficient photoelectrochemical water splitting, Nano Lett. 11 (5) (2011) 1928–1933.

[13] S.J. Hong, S. Lee, J.S. Jang, J.S. Lee, Heterojunction BiVO₄/WO₃ electrodes for enhanced photoactivity of water oxidation, Energy Environ. Sci. 4 (5) (2011) 1781–1787.

[14] S.Y. Chae, C.S. Lee, H. Jung, O.S. Joo, B.K. Min, J.H. Kim, Y.J. Hwang, Insight into charge separation in WO3/BiVO4 heterojunction for solar water splitting, ACS Appl. Mater. Interfaces 9 (23) (2017) 19780–19790.

[15] I. Grigioni, K.G. Stamplecoskie, E. Selli, P.V. Kamat, Dynamics of photogenerated charge carriers in WO₃/BiVO₄ heterojunction photoanodes, J. Phys. Chem. C 119 (36) (2015) 20792–20800.

[16] J.H. Kim, J.W. Jang, Y.H. Jo, F.F. Abdi, Y.H. Lee, R. Van De Krol, J.S. Lee, Hetero-type dual photoanodes for unbiased solar water splitting with extended light harvesting, Nat Commun. 7 (1) (2016) 1–9.

[17] K. Zhang, M. Ma, P. Li, D.H. Wang, J.H. Park, Water splitting progress in tandem devices: moving photolysis beyond electrolysis, Adv Energy Mater 6 (15) (2016), 1600602.

[18] G. Cai, J. Tu, D. Zhou, J. Zhang, Q. Xiong, X. Zhao, X. Wang, C. Gu, Multicolor electrochromic film based on TiO₂@ polyaniline core/shell nanorod array, J. Phys. Chem. C 117 (31) (2013) 15967–15975.

[19] D. Hidalgo, S. Bocchini, M. Fontana, G. Saracco, S. Hernandez, Green and low-cost synthesis of PANI–TiO₂ nanocomposite mesoporous films for photoelectrochemical water splitting, RSC Adv. 5 (61) (2015) 49429–49438.

[20] W. Kong, X. Zhang, S. Liu, Y. Zhou, B. Chang, S. Zhang, H. Fan, B. Yang, N doped carbon dot modified WO₃ nanoflakes for efficient photoelectrochemical water oxidation, Adv. Mater. Interfaces 6 (1) (2019), 1801653.

[21] H. Qi, J. Wolfe, D. Wang, H.J. Fan, D. Fichou, Z. Chen, Triple-layered nanostructured WO₃ photoanodes with enhanced photocurrent generation and superior stability for photoelectrochemical solar energy conversion, Nanoscale 6 (22) (2014) 13457–13462.

[22] S. Khoomortezaei, H. Abdizadeh, M.R. Golobostanfard, Triple layer heterojunction WO₃/BiVO₄/BiFeO₃ porous photoanode for efficient photoelectrochemical water splitting, ACS Appl. Energy Mater. 2 (9) (2019) 6428–6439.

[23] T. Zhou, S. Chen, J. Wang, Y. Zhang, J. Li, J. Bai, B. Zhou, Dramatically enhanced solar-driven water splitting of BiVO₄ photoanode via strengthening hole transfer and light harvesting by co-modification of CQDs and ultrathin β-FeOOH layers, Chem. Eng. J. 403 (2021), 126350.

[24] R. Keshavarzi, N. Molabahrami, N. Afzali, M. Omrani, Improving efficiency and stability of carbon-based perovskite solar cells by a multifunctional triple-layer system: antireflective, uv-protective, superhydrophobic, and self-cleaning, Solar RRL 4 (12) (2020), 2000491.

[25] M.T. Masood, S. Qudsia, M. Hadadian, C. Weinberger, M. Nyman, C. Ahläng, S. Dahlström, M. Liu, P. Vivo, R. Österbacka, Investigation of well-defined pinholes in TiO₂ electron selective layers used in planar heterojunction perovskite solar cells, Nanomaterials 10 (1) (2020) 181.

[26] K. Majid, S. Awasthi, M. Singla, Low temperature sensing capability of polyaniline and Mn₃O₄ composite as NTC material, Sens. Actuators A Phys. 135 (1) (2007) 113–118.

[27] A. MacDiarmid, A. Epstein, Polyanilines: from solitons to polymer metal, from chemical currosity to technology, Synth. Met. 69 (1995) 179.

[28] Y. Liang, T. Tsubota, L.P. Mooij, R. van de Krol, Highly improved quantum efficiencies for thin film BiVO₄ photoanodes, J. Phys. Chem. C 115 (35) (2011) 17594–17598.

[29] M.C. Haven, G.A. Tetrault, J.R. Schenken, Laboratory Instrumentation, John Wiley & Sons, 1994.

[30] M. Omrani, H. Fallah, K.L. Choy, M. Abdi-Jalebi, Impact of hybrid plasmonic nanoparticles on the charge carrier mobility of P3HT: PCBM polymer solar cells, Sci. Rep. 11 (1) (2021) 1–12.

[31] B. AlOtaibi, S. Fan, S. Vanka, M. Kibria, Z. Mi, A metal-nitride nanowire dual-photoelectrode device for unassisted solar-to-hydrogen conversion under parallel illumination, Nano Lett. 15 (10) (2015) 6821–6828.

[32] C. Ding, W. Qin, N. Wang, G. Liu, Z. Wang, P. Yan, J. Shi, C. Li, Solar-to-hydrogen efficiency exceeding 2.5% achieved for overall water splitting with an all earth-abundant dual-photoelectrode, Phys. Chem. Chem. Phys. 16 (29) (2014) 15608–15614.

[33] S. Xu, D. Fu, K. Song, L. Wang, Z. Yang, W. Yang, H. Hou, One-dimensional WO₃/BiVO₄ heterojunction photoanodes for efficient photoelectrochemical water splitting, Chem. Eng. J. 349 (2018) 368–375.

[34] H.W. Jeong, T.H. Jeon, J.S. Jang, W. Choi, H. Park, Strategic modification of BiVO₄ for improving photoelectrochemical water oxidation performance, J. Phys. Chem. C 117 (18) (2013) 9104–9112.

[35] B. Klahr, S. Gimenez, F. Fabregat-Santiago, J. Bisquert, T.W. Hamann, Photoelectrochemical and impedance spectroscopic investigation of water oxidation with "Co-Pi"-coated hematite electrodes, J. Am. Chem. Soc. 134 (40) (2012) 16693–16700.

[36] P. Kong, P. Liu, Z. Ge, H. Tan, L. Pei, J. Wang, P. Zhu, X. Gu, Z. Zheng, Z. Li, Conjugated HCl-doped polyaniline for photocatalytic oxidative coupling of amines under visible light, Catal. Sci. Technol. 9 (3) (2019) 753–761.

[37] J. Wang, J. Huang, J. Meng, Q. Li, J. Yang, Enhanced photoelectrochemical performance of anatase TiO₂ for water splitting via surface codoping, RSC Adv. 7 (63) (2017) 39877–39884.

[38] S. Ashokan, V. Ponnuswamy, P. Jayamurugan, J. Chandrasekaran, Y.S. Rao, Influence of the counter ion on the properties of organic and inorganic acid doped polyaniline and their Schottky diodes, Superlattices Microstruct. 85 (2015) 282–293.

[39] S. Wang, S. Lu, X. Li, X. Zhang, S. He, T. He, Study of H₂SO₄ concentration on properties of H₂SO₄ doped polyaniline counter electrodes for dye-sensitized solar cells, J. Power Sources 242 (2013) 438–446.

[40] S. Badilescu, P. Ashrit, Study of sol–gel prepared nanostructured WO₃ thin films and composites for electrochromic applications, Solid State Ion. 158 (1–2) (2003) 187–197.

[41] R. Keshavarzi, V. Mirkhani, M. Moghadam, S. Tangestaninejad, I. Mohammadpoor-Baltork, Highly efficient dye sensitized solar cells based on ordered and disordered mesoporous titania thick templated films, J. Mater. Chem. A 3 (5) (2015) 2294–2304.

[42] M. Zukalova, A. Zukal, L. Kavan, M.K. Nazeeruddin, P. Liska, M. Grätzel, Organized mesoporous TiO₂ films exhibiting greatly enhanced performance in dye-sensitized solar cells, Nano Lett. 5 (9) (2005) 1789–1792.

[43] J.H. Pan, X. Zhao, W.I. Lee, Block copolymer-templated synthesis of highly organized mesoporous TiO₂-based films and their photoelectrochemical applications, Chem. Eng. J. 170 (2–3) (2011) 363–380.

[44] R. Djara, Y. Holade, A. Merzouki, M.A. Lacour, N. Masquelez, V. Flaud, D. Cot, B. Rebiere, A. van der Lee, J. Cambedouzou, Nanostructured carbon-nitrogen-sulfur-nickel networks derived from polyaniline as bifunctional catalysts for water splitting, Front. Chem. 8 (2020) 385.

[45] G. Wang, Z. Yang, X. Li, C. Li, Synthesis of poly (aniline-co-o-anisidine)-intercalated graphite oxide composite by delamination/reassembling method, Carbon N Y 43 (12) (2005) 2564–2570.